Cellular/Molecular

Presynaptic Vesicles Supply Membrane for Axonal Bouton Enlargement during Long Term Potentiation

L. M. Kirk,[1] G. C. Garcia,[2] D. C. Hanka,[1] K. Zatyko,[1] T. Bartol,[2] T. J. Sejnowski,[2,3] and K. M. Harris[1]

[1]Center for Learning and Memory, Department of Neuroscience, University of Texas at Austin, Austin, Texas 78712, [2]Computational Neurobiology Laboratory, The Salk Institute for Biological Studies, La Jolla, California 92037, and [3]Division of Biological Sciences, University of California, San Diego, La Jolla, California 92093

Long-term potentiation (LTP) induces presynaptic bouton enlargement and a reduction in the number of synaptic vesicles. To understand the relationship between these events, we performed 3D analysis of serial section electron micrographs in hippocampal area CA1 from male rats, 2 h after LTP induction. We observed a high vesicle packing density in control boutons, contrasting with a lower density in most LTP boutons. Notably, the summed membrane area of the vesicles lost in low-density LTP boutons is comparable to the surface membrane required for the observed bouton enlargement when compared with high-density control boutons. These novel findings suggest that presynaptic vesicle density provides a new structural indicator of LTP that supports a local mechanism of bouton enlargement.

Key words: **bouton; hippocampus; LTP; presynaptic vesicle; synapse; ultrastructure**

Significance Statement

This research reveals how neurons physically change during plasticity events. We show that long-term potentiation causes presynaptic boutons to enlarge, using membrane recycled from lost neurotransmitter-containing vesicles. This discovery provides a new structural indicator of synaptic plasticity and insights into how synapses are dynamically reorganized, impacting our understanding of learning and memory, and potentially neurological disorders.

Introduction

For animals to learn and remember new information, synapses must remain in a modifiable, plastic state. A widely recognized cellular basis for learning and memory is long-term potentiation (LTP), a type of synaptic plasticity that refers to the sustained strengthening of synaptic connections that occurs after brief high frequency stimulation (Bliss and Gardner-Medwin, 1973). Synapses are strengthened postsynaptically through insertion of new glutamate receptors into the postsynaptic membrane (Choquet, 2018; Buonarati et al., 2019), while presynaptically there is an increase in the release probability (P_r; Neher and Brose, 2018; Harris, 2025). While these changes occur rapidly after LTP induction, they are sustained for hours and are accompanied by structural changes (Sokolov et al., 2002; Jung et al., 2021).

By 2 h, dendritic spines and their excitatory synapses are enlarged at the expense of smaller neighboring spines (Bourne and Harris, 2011). Presynaptic boutons, the sites of neurotransmitter release, also undergo structural modifications during LTP (Harris, 2025). Superresolution imaging of CA3 axons in organotypic slices revealed that boutons were enlarged shortly following LTP induction by high frequency stimulation and remained enlarged for the duration of the experiment (Chéreau et al., 2017). Two hours following LTP induction in acute hippocampal slices, there is a decrease in total bouton number compared with control stimulation, which occurs primarily by losing single synaptic and nonsynaptic boutons (Smith et al., 2016). In the remaining LTP boutons, both docked and nondocked vesicle counts were decreased at 2 h compared with control boutons (Bourne et al., 2013; Smith et al., 2016). Considering synaptic vesicles are the source of neurotransmitter release, it is perhaps surprising that an increase in P_r is accompanied by a decrease in synaptic vesicles. However, during LTP, more of the vesicles at the active zone are tightly docked (Jung et al., 2021), likely representing vesicles that are primed and in a readily

Received July 11, 2025; revised March 18, 2026; accepted April 19, 2026.

Author contributions: L.M.K., T.J.S., and K.M.H. designed research; L.M.K., D.C.H., and K.Z. performed research; T.B. contributed unpublished reagents/analytic tools; L.M.K., G.C.G., D.C.H., and K.Z. analyzed data; L.M.K. wrote the paper.

This work was supported by the National Institutes of Health grants R01MH095980 and R56MH139176, and National Science Foundation NeuroNex grants 2014862 and 2219894 to K.M.H. We thank Patrick Parker for proofreading and helpful suggestions on the manuscript.

The authors declare no competing financial interests.

Correspondence should be addressed to L. M. Kirk at lyndskirk@utexas.edu.

This paper contains supplemental material available at: https://doi.org/10.1523/JNEUROSCI.1335-25.2026

https://doi.org/10.1523/JNEUROSCI.1335-25.2026

releasable state (Neher and Brose, 2018). Regardless, the destination of the lost vesicles during LTP remained unclear. Although small transport packets of synaptic vesicles can translocate between neighboring boutons as part of a larger "super pool" (Fernandez-Alfonso and Ryan, 2008), transport packets are decreased 2 h following LTP (Bourne et al., 2013), and potentiation does not require recruitment of extrasynaptic vesicles (Ratnayaka et al., 2012). Here, we propose that the membrane from lost synaptic vesicles provides the required increase in surface area for the enlarged presynaptic boutons during LTP. To test this hypothesis, we developed new tools that obtain accurate quantification of object surface areas through 3D reconstruction from serial section electron microscopy (3DEM).

Materials and Methods

Animals. Serial section images were analyzed from series that had been prepared for prior publications as described below. Procedures were carried out in accordance with the National Institutes of Health guidelines for the humane care and use of laboratory animals. All protocols and procedures involving animals were approved by the Institutional Animal Care and Use Committee at The University of Texas at Austin. All 3DEM data were collected from adult male Long–Evans rats.

Physiology. Slice preparation and physiology were previously described and published (Bourne and Harris, 2011; Bourne et al., 2013). Adult male Long–Evans rats aged 60–61 d old were anesthetized with halothane and decapitated, and 400-µm-thick slices were rapidly collected from the middle third of the hippocampus at room temperature using a Stoelting tissue chopper. Slices were recovered in a humidified interface chamber using artificial cerebrospinal fluid for ∼3 h at 32°C. For experiments where LTP was blocked, 50 µM APV (D-2-amino-5-phosphonopentanoic acid; Sigma-Aldrich) was added into the interface chambers at the end of the 3 h recovery period and remained for the duration of the experiment (Fig. 2*c*). One extracellular recording electrode was placed in the middle of stratum radiatum, and two bipolar stimulating electrodes were placed ∼300–400 µm on either side of the recording electrode (Fig. 2*a*). An input–output curve was generated, and the initial slope of the field excitatory postsynaptic potential (fEPSP) was measured. The stimulus intensity was set at 75% of the maximum fEPSP, just below the population spike threshold, and held constant throughout the experiment. Stimulations were delivered once every 2 min, with a 30 s lag between control and LTP stimulation electrodes. Baseline fEPSPs were collected for 30 min before theta-burst stimulation (TBS: 8 trains spaced at 30 s intervals, with each train consisting of 10 bursts at 5 Hz, and each burst consisting of 4 pulses at 100 Hz) was delivered to one stimulating electrode to produce LTP (Fig. 2*b*,*c*). The fEPSPs were recorded in response to alternating control and LTP test pulses for 2 h. The sites of LTP versus control stimulation (near CA3 or subiculum) alternated between experiments.

Tissue fixation, processing, and imaging. Fixation, processing, and imaging methods were previously described and published (Bourne and Harris, 2011). Briefly, electrodes were removed, and slices were rapidly fixed by immersing them into mixed aldehydes (6% glutaraldehyde, 2% paraformaldehyde in 100 mM cacodylate buffer with 2 mM $CaCl_2$ and 4 mM $MgSO_4$) and microwaving for 10 s. Slices were then stored in the same fixative overnight at room temperature before being embedded in 7% agarose and then vibra-sliced at 70 µm (Leica VT 1000S, Leica). Vibra-slices that showed a visible surface indentation from the stimulation electrodes along with two adjacent vibra-slices were identified and processed using the following procedure: 1% osmium/1.5% potassium ferrocyanide mixture, 1% osmium alone, dehydrated through graded ethanol (50–100%), and propylene oxide, embedded in LX112, and placed in a 60°C oven for 48 h.

Test thin sections were cut from regions located 150–00 µm lateral to the stimulating electrodes and 120–150 µm beneath the air surface of the slice and mounted on Pioloform-coated slot grids (SynapTek, Ted Pella). Sections were counterstained with saturated ethanolic uranyl acetate and Reynolds lead citrate and imaged on a JEOL 1230 electron microscope with a Gatan digital camera at 5,000× magnification. Images were then assessed for quality of tissue preservation. Approximately 200 serial sections were then cut and imaged, and a five-letter code was used to mask the identity of experimental conditions in subsequent analyses. A diffraction grating replica (Ernest Fullam) was imaged with each series to calibrate *x*–*y* dimensions.

In silico ultramicrotome. The in silico ultramicrotome is a software tool designed to assess the accuracy of the reconstruction pipeline starting from hand-tracing of the electron microscopy (EM) images through the final step of mesh generation. It is an open-source Python script built on top of Blender, a popular 3D CAD/CGI platform. Ground truth values for accuracy testing of our reconstruction methods were established by generating surface meshes from densely segmented hippocampal neuropil (Harris et al., 2015) in Blender, using NeuropilTools and Contour Tiler, and calculating surface areas for each object (Fig. 1*a*). These objects were resectioned using the in silico ultramicrotome to create wire-framed virtual sections of known thickness (Fig. 1*b*). Simulated membranes were then added to objects to create virtual electron micrographs (Fig. 1*c*). Objects in the virtual micrographs can then be retraced (Fig. 1*d*), their meshes regenerated, and their surface areas compared with ground truth values.

Unbiased axon selection and segmentation. Series were initially aligned, and five dendrites of similar caliber and their synapses were previously segmented using legacy Reconstruct software (Fiala, 2005; Bourne and Harris, 2011). Section thickness was computed by dividing the diameters of longitudinally sectioned mitochondria by the number of sections they spanned (Fiala and Harris, 2001). Series were then imported into PyReconstruct (Chirillo et al., 2025). For each dendrite, the middle 15 excitatory spine synapses were identified, and their axons were traced. Most axons traverse the neuropil in a winding fashion, meaning their membranes are often not cut in cross section and their edges are ambiguous to discern. We used the in silico ultramicrotome to test different segmentation methods and found that the most accurate segmentation could be achieved by including gray wall membrane that overlapped with cytoplasm on adjacent sections (Fig. 1*d*,*e*). Axonal boutons were traced to a sufficient distance to capture both the target bouton and adjacent interbouton regions. If the axon made another bouton nearby, then that bouton and its synapses were also traced. Any additional PSDs that contacted the traced boutons were segmented. Both docked and nondocked vesicles were stamped, and mitochondria were traced.

Bouton measurement in NeuropilTools. Axon traces were imported from Reconstruct into Blender as contours using NeuropilTools in CellBlender (a modeling plug-in for Blender; Bartol et al., 2015). The contours were converted into a three-dimensional mesh using NeuropilTools via its Contour Tiler module. The resulting mesh was then improved using the GAMer module to smooth the mesh and remove distortions. Synaptic contact areas were tagged (via the obj_tag_region module) onto the axon surface areas and nondocked synaptic vesicles and mitochondria were imported for visualization. Two experimenters, masked as to condition, examined each axon in 3D to assess morphology from all angles. The lasso tool (included in NeuropilTools) was used to select the bouton region (Fig. 1*g*,*i*). Bouton ends were defined as the region where constriction ceased, and a relatively uniform tubular circumference was maintained along the axon (interbouton region). The mitochondria, vesicles, and synapses provided additional context, especially along the slopes between the axonal bouton and interbouton regions. Each experimenter measured each bouton twice, and intra- and intertracer errors were determined for the surface area. When measurement error was above 10%, the bouton was reviewed by both tracers in tandem to determine the cause of the discrepancy. Boutons exhibiting ambiguous morphology, such as those appearing to merge or split, were excluded from analysis. The average intratracer error

was 2.04% ± 0.08, and the average intertracer error was 2.43% ± 0.14. The average of the four surface area measurements was used for analysis.

Vesicle surface area measurements. Although all synaptic vesicles within the selected boutons were identified, stamped, and counted, only a subset of vesicles were manually segmented to obtain their surface areas. Because we used circumference to calculate the surface area, it was important to only include vesicles that were circular in shape, clearly distinguishable from other vesicles, and were fully contained within a single section (which tend to appear with a distinct membrane and a clear lumen; Fig. S4*a–c*). To sample from the range of bouton sizes and conditions for vesicle measurement, axonal boutons from each series were first categorized by the presence of mitochondria. Each population was then ranked by bouton surface area and placed into 10% bins. A bouton was randomly selected from each bin, and if it contained a minimum of 10 vesicles that met our criteria, the vesicles were segmented and the circumference used to calculate spherical surface area. If a selected bouton did not contain at least 10 vesicles matching our criteria, another was selected from the same size bin instead. A total of 30 boutons containing mitochondria and 30 boutons lacking mitochondria in each series had their vesicles traced (Fig. S4*d*; $n = 8$ series, 480 boutons, 8,629 vesicles).

Distance of neighboring vesicles. To compute the distance between neighboring vesicles, we used the Delaunay triangulation associated with the vesicle cluster. The triangulation was generated using the associated routine in SciPy 1.1.0 through a Python script written for Blender 2.79. The Euclidean distances between neighboring vesicles (i.e., vesicles connected in the Delaunay triangulation) were calculated and the mean distance was computed for each vesicle. Because the distribution of mean vesicle distances within each cluster was skewed, the median was reported for each bouton. Finally, we obtained a membrane-to-membrane distance by subtracting two times the median vesicle radius for each series (see above, Vesicle surface area measurements).

Modeled bouton growth. The summed vesicle surface area per bouton was calculated by multiplying each bouton's vesicle number (Fig. 2*f*) by the median vesicle surface area of the originating series (Fig. S4*d*). Outliers were defined as values exceeding three times the interquartile range (IQR) beyond the lower and upper quartiles for both summed vesicle surface area and bouton surface area. Using these criteria, three data points were removed from the control condition and one from the LTP. Bouton surface areas were then plotted against summed vesicle surface areas. We used GraphPad Prism 10 to determine model II Major Axis linear regressions, suitable when both x and y variables are in the same units and subject to measurement error. For comparison of variable relationships between LTP and Modeled Growth, we first tested for the homogeneity of slopes using the F test on the interaction term. The slopes were not significantly different, so we proceeded to test for differences in the elevations (y-intercepts) of the lines. This allowed us to determine if the groups differed significantly in their y values after accounting for the influence of the x variable.

Experimental design and statistical analysis. As described above, control and TBS were induced within the same hippocampal slice to control for variation across animals. Two animals (one hippocampal slice per animal) were used for each experiment (TBS vs Control; TBS vs Control in the presence of APV). Slices were fixed 2 h following stimulation, and tissue was taken near the stimulating electrode to maximize analysis for stimulated axons. To control for variation in stimulus location, the sites of LTP versus control stimulation (near CA3 or subiculum) alternated between experiments. For each condition, the middle 15 excitatory synapses from 5 dendrites of similar caliber were identified, and their axons were traced.

Analysis of covariance (ANCOVA) was used to test for differences in vesicle counts between control and LTP conditions across bouton surface areas (Fig. 2, Fig. S3). Because both vesicle counts and bouton surface areas have skewed distributions, data were log10 transformed prior to analysis. Statistica [TIBCO Software Inc. (2020), Data Science Workbench, version 14, http://tibco.com] was used to first test for ANCOVA assumptions (Levine's test for homogeneity of variances, homogeneity of slopes). In Figure S3*d*, Levine's test showed a slightly significant difference in variance ($p = 0.045$). However, we had roughly equal sample sizes between conditions, and the variance ratio was <4 (1.5), so we determined this to be a minor violation and continued with the ANCOVA analysis. Although ANCOVAs were performed on log transformed data, the raw data points were plotted on log axes with a power regression in Microsoft Excel to visualize the skewed nature of the raw data and the linear relationships.

GraphPad Prism was used for all other statistical analyses (version 10.3.1 for Window; www.graphpad.com). In Figure 3*d*, frequency distributions for the median distance to neighboring vesicles per bouton were determined using 2.5 nm bins. Relative frequency histograms were then created using second-order smoothing (four neighbors). The Mann–Whitney test was used for all pairwise comparisons. For all figures, $*p < 0.05$, $**p < 0.01$, $***p < 0.001$, $****p < 0.0001$.

Results

Accurate segmentation and quantification of axon surface areas

Accurate measurement of membrane surface area through serial section electron microscopy required a new approach to account for the overlap between obliquely sectioned objects. Membranes of adjacent processes are thin enough (~15 nm) to overlap within the same ultrathin section (~50 nm) when cut obliquely and thus produce an ambiguous gray surface. An in silico ultramicrotome was developed to determine how to assign ambiguous membranes to adjacent structures (Fig. 1). Overlapping objects from densely segmented neuropil (Harris et al., 2015) were resectioned virtually to produce membrane boundaries with known surface areas (Fig. 1*a–d*). Accurate surface areas are achieved by assigning the gray surface area to the axon with overlapping cytoplasm on the adjacent sections (Fig. 1*d*,*e*). Although the membrane surface area of perfectly cross-sectioned boutons can be readily calculated by measuring the perimeter on each section and multiplying by section thickness (Fig. 1*f–g*), most axons are not perfectly cross-sectioned (Fig. 1*h*,*i*). Thus, the new method allowed an unbiased inclusion of both cross-sectioned and obliquely sectioned axons to determine the impact of LTP on the membrane surface area of presynaptic boutons.

Vesicles are lost as boutons enlarge during LTP

Acute hippocampal slices were recovered for at least 3 h to allow ultrastructure to return to its in vivo appearance (Fiala et al., 2003). Two stimulating electrodes and one recording electrode were placed in the middle of CA1 stratum radiatum (Fig. 2*a*). LTP was induced at one of the electrodes using theta-burst stimulation, and the other electrode received test pulses only as a control (Bourne and Harris, 2011; Fig. 2*b*). In separate slices, LTP was blocked with bath application of 50 μM APV, an NMDA receptor antagonist (Fig. 2*c*). At 2 h, the slices were rapidly fixed in aldehydes, and tissue near the stimulating electrodes was harvested and processed for serial section EM (Bourne and Harris, 2011).

Small synaptic vesicles were located and counted, presynaptic mitochondria and synapses (defined by surface area of the PSD) were segmented, and axonal boutons were delineated along reconstructed excitatory axons (Fig. 2*d*,*e*,*i*,*j*; Figs. S1 and S2). Total vesicle numbers per bouton decreased with LTP (Fig. 2*f*), and bouton surface areas were increased (Fig. 2*g*). Vesicle numbers and bouton surface areas were positively correlated in both control and LTP conditions, and the drop in vesicle numbers occurred across all bouton sizes after LTP (Fig. 2*h*). Prior work using STED microscopy suggests that the axonal shaft between

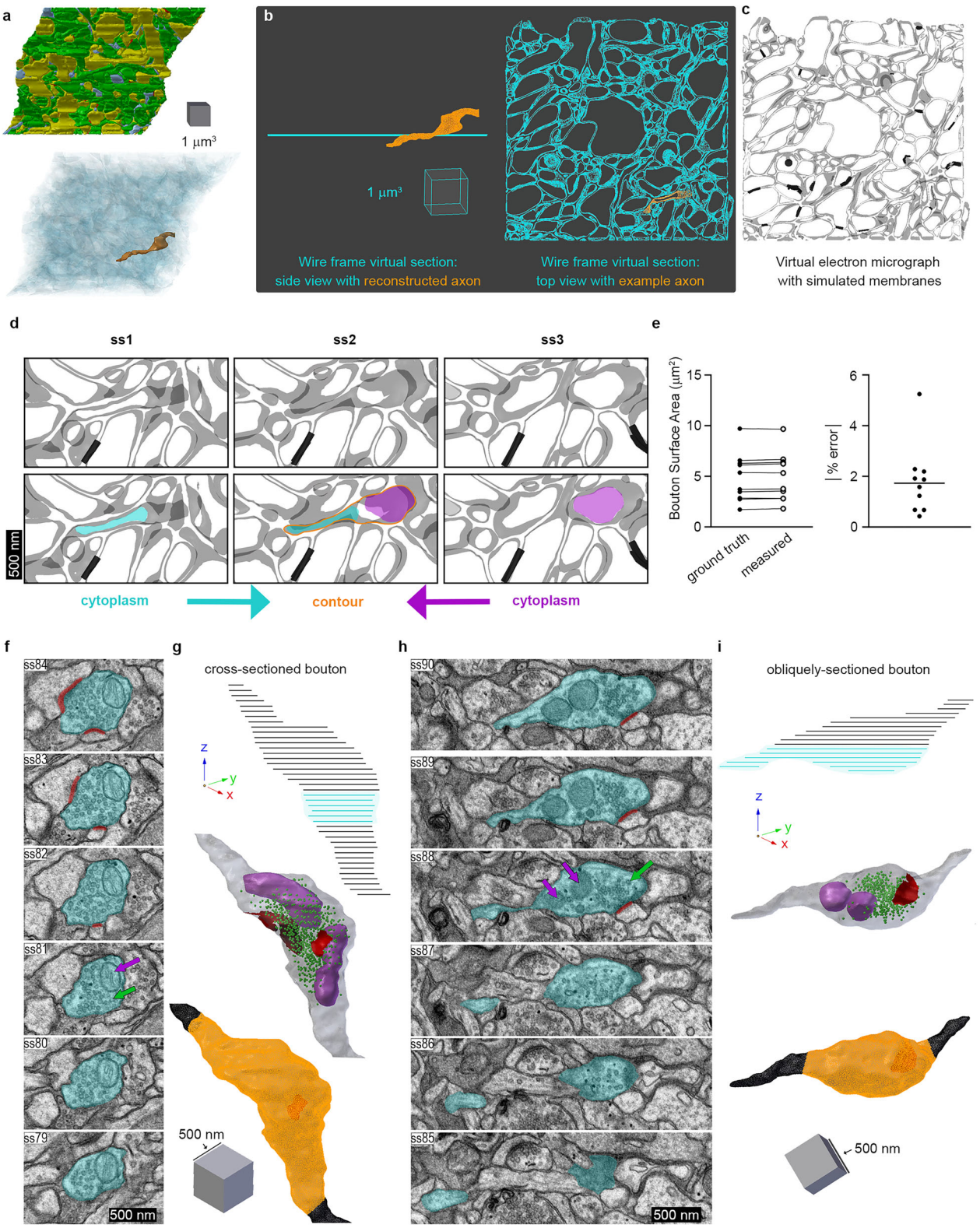

Figure 1. Accurate segmentation and quantification of axon surface areas. ***a***, Reconstructed volume containing fully segmented objects from serial section EM (top). Surface meshes were generated using NeuropilTools. A sample axon is shown in orange with the remaining objects in transparent teal (bottom). ***b***, Side view and top-down view of one virtual section that was created using the in silico ultramicrotome. ***c***, Virtual electron micrograph with simulated membranes for each object in ***b***. ***d***, Segmentation strategy using cytoplasm from adjacent serial sections (ss1 and ss3) to guide the amount of gray wall to include in the contour on ss2. ***e***, This segmentation strategy resulted in no significant difference between the ground truth values and the manually measured surface area of axons in the virtual volumes (median absolute error = 1.7%, $n = 10$ axonal boutons). Serial section EM images and 3D reconstructions show example segmentation (teal) of cross-sectioned (***f***, ***g***) and obliquely sectioned (***h***, ***i***) axons, demonstrating how the new segmentation strategy was applied to obtain accurate surface areas. Excitatory postsynaptic densities (red), mitochondria (purple arrows), and synaptic vesicles (green arrows) are also indicated in EM images. ***g***, ***i***, Top, Axon contours are shown traversing through the *z*-axis, and the teal lines indicate the contours shown in the EM example images in ***f*** and ***h***. Middle, 3D meshes of the axons are generated and smoothed using NeuropilTools. Axons contain synapses (red), presynaptic vesicles (green), and mitochondria (purple). Bottom, The region of each axon used to calculate bouton surface area is indicated in orange, and interbouton regions are black.

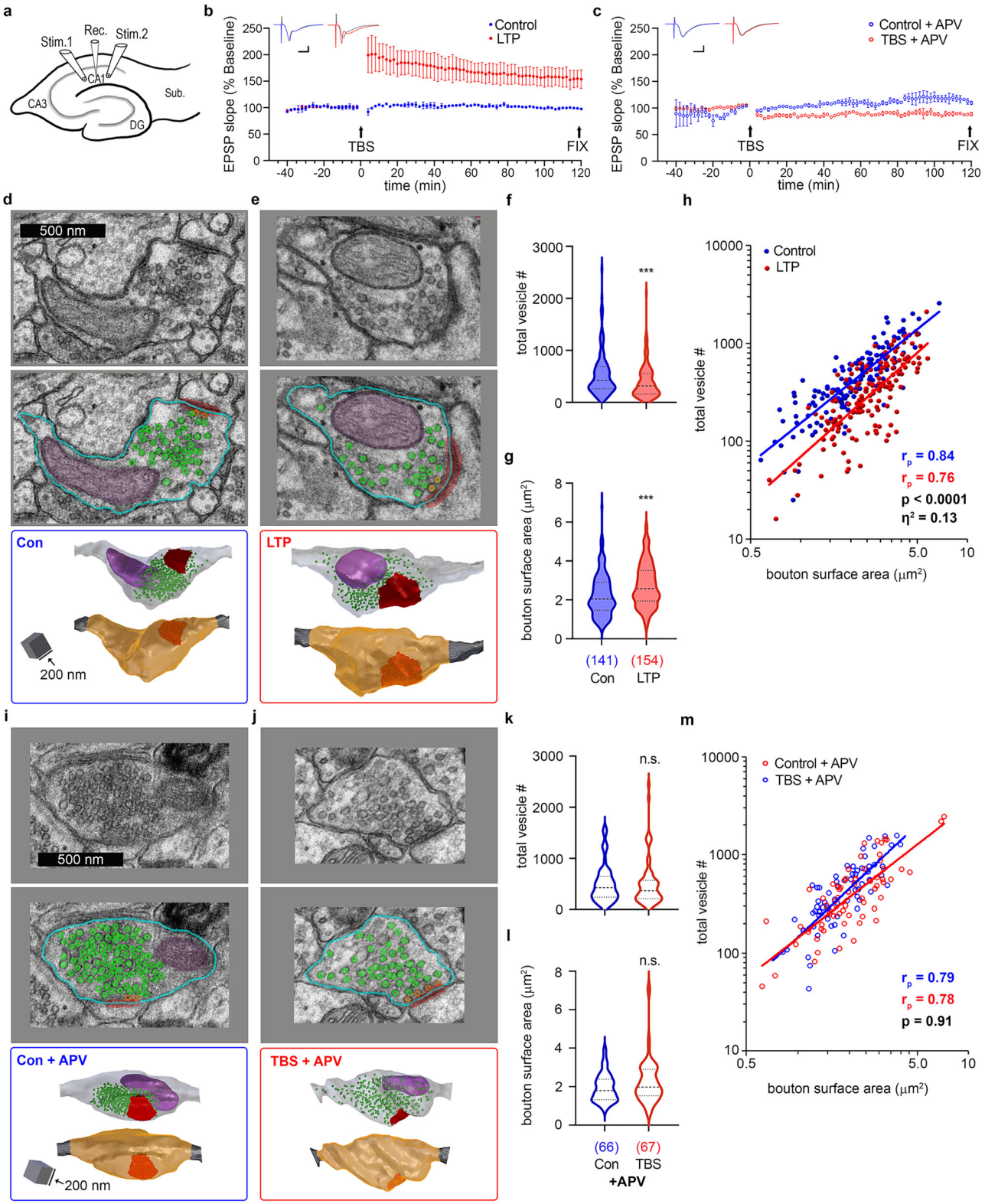

Figure 2. Presynaptic vesicle numbers are decreased, and boutons are larger following LTP. ***a***, Diagram of acute hippocampal slice with one recording electrode and two stimulating electrodes delivering alternating stimuli. ***b***, EPSP slope increased after theta-burst stimulation (TBS) delivered at $t = 0$ min and was maintained for 2 h (LTP, red). Test-pulse stimulation does not increase the EPSP (Control, blue). The inset shows average waveforms over 10 min from baseline (black; $t = -10$–0 min) and after TBS or control stimulation (red/blue; $t = 110$–120 min). ***c***, Bath application of 50 μM APV prevents LTP induction with TBS stimulation. For ***b*** and ***c*** $n = 2$ animals per condition, and error bars show SEM. Inset calibration: $x = 5$ ms and $y = 10$ mV. ***d–e***, Electron micrographs, segmentations, and 3D reconstructions representing the median vesicle numbers and bouton surface areas for control (***d***) and LTP (***e***). In addition to axon segmentation (teal), postsynaptic density (red) and mitochondria (purple) segmentations are shown. Docked (orange) and nondocked (green) vesicles are also identified. ***f***, Total vesicle number per bouton is decreased with LTP ($p = 0.0005$). ***g***, Bouton surface areas are increased with LTP ($p = 0.0001$). ***h***, Presynaptic vesicle numbers are positively correlated with bouton surface area in both control and LTP conditions (r_p = Pearson's R, $p < 0.0001$). Boutons in the LTP condition have fewer presynaptic vesicles compared with control with an effect size (partial eta-squared) of 13% attributed to condition (ANCOVA: $F_{condition} = 42$; df = 1; $p < 0.0001$). For ***f–h***, n(Con) = 141 and n(LTP) = 154. ***i***, ***j***, Electron micrographs, segmentations, and 3D reconstructions representing the median

boutons may also expand after LTP (Chéreau et al., 2017). We performed a targeted analysis of axonal shafts by measuring interbouton regions between pairs of complete boutons fully captured within the serial section EM volume (Fig. S3*a*). The mean cross-sectional area of the interbouton region was determined for each axon by computing the total interbouton volume normalized across its reconstructed length. Within this subset of segments, no significant differences in the cross-sectional area were detected between control and LTP conditions (Fig. S3*b*).

When LTP was blocked with APV, there were no differences in vesicle numbers (Fig. 2*k*) or bouton surface areas (Fig. 2*l*) between control and TBS conditions. While vesicle numbers and bouton surface areas were still positively correlated, the relationship between vesicle numbers and bouton surface areas did not differ across the APV control and TBS conditions (Fig. 2*m*). These results indicate that the decrease in presynaptic vesicle number and concurrent increase in bouton surface area require NMDA receptor activation and LTP.

Decreased vesicle density as a novel structural indicator of LTP

In many of the LTP boutons, nondocked presynaptic vesicles appeared to be spaced farther apart than in the control boutons (Figs. S1, S2). To determine whether these spatial relationships were significantly different, a Delaunay mesh was constructed that connected the center points of the vesicles within a bouton (Fig. 3*a*,*b*). All vesicles could be counted by viewing them through serial sections and distinguishing them from other membrane bound organelles (e.g., smooth endoplasmic reticulum and endosomes). However, some vesicle circumferences could not be measured if their bounding membranes were incomplete or their shape was not spherical. Thus, only the spherical presynaptic vesicles that had an evenly stained membrane with a clear lumen were included to calculate the median vesicle size (see Materials and Methods; Fig. S4). The median vesicle radius for each series was then used to calculate the membrane-to-membrane distances from each vesicle to all neighboring vesicles (d_1, d_2, d_3… d_n) for each nondocked vesicle (v) in the bouton (Fig. 3*c*). The average distance to neighboring vesicles, or DNV, was then determined for each nondocked vesicle (v) within a bouton:

$$\mathrm{DNV(v)} = \overline{d_n} - 2r,$$

where

$$\overline{d_n} = \text{mean distance } (d_1,\ d_2 \ldots d_n) \text{ to neighboring vesicles}(v_1,\ v_2 \ldots v_n) \text{ per vesicle } (v),$$

$$r = \text{median vesicle radius per series.}$$

The median DNV was found for each bouton and their relative frequencies plotted for each condition (Fig. 3*d*). Then the value at which the control and LTP curves intersected (0.035 µm) was set as the boundary between boutons with high and low vesicle densities (Fig. 3*d*). In line with our visual observations, there were more LTP boutons with low vesicle densities than in any other condition. Boutons containing comparable vesicle numbers illustrate that the observed high or low vesicle density is not solely determined by the absolute vesicle number (Fig. 3*e*). Mitochondria-containing boutons generally have more vesicles (Fig. S3). However, the presence of a mitochondrion did not affect the proportion of boutons with high or low vesicle densities (Fig. 3*e*, Fig. S4*e*). The proportion of single synaptic and multisynaptic boutons that had high and low vesicle densities also did not differ between the LTP and control conditions (Fig. S4*f*). Hence, subsequent analyses combined results from all types of presynaptic boutons with and without mitochondria.

Synaptic structures such as boutons, PSDs, and dendritic spines scale proportionally in size, including following potentiation (Meyer et al., 2014). Here we examined whether vesicle density, a novel structural indicator of LTP, would stratify this relationship by comparing control boutons with high vesicle density against LTP boutons with low vesicle density. The correlation between bouton surface area and total synapse area (summed across synapses on MSBs) remained similarly strong across both groups (Fig. 3*f*), suggesting that presynaptic bouton growth scales proportionally with synapse size despite an LTP-dependent decrease in nondocked vesicle density.

Vesicle membrane contribution to presynaptic bouton growth in LTP

We hypothesize that the membrane from the lost synaptic vesicles is used to grow presynaptic boutons during late-phase LTP (Fig. 4*a*). To test this hypothesis, the summed vesicle surface area per bouton was plotted versus the bouton surface area, and the control regression was subtracted from the LTP regression to find the lost vesicle surface area (SA; Fig. 4*b*):

$$\text{Lost vesicle SA } (\mu m^2) = y_{\mathrm{Ctrl}} - y_{\mathrm{LTP}},$$

where

$$y_{\mathrm{Ctrl}} = 2.23x - 2.30,$$

$$y_{\mathrm{LTP}} = 1.75x - 2.56,$$

$$\text{Lost Vesicle SA } (\mu m^2) = 0.476x - 0.265.$$

The lost vesicle SA equation was derived to predict the summed vesicle surface area that would be lost for every control bouton in our dataset if it were to undergo LTP. To model bouton growth, the calculated lost vesicle surface area was then added to each control bouton surface area. Because we are only measuring unidirectional and unrestricted bouton growth and we know there is a biological ceiling to bouton size, we only plotted modeled boutons that fell within our measured range (Fig. 4*c*, modeled growth). While the membrane from the lost vesicles was sufficient to account for the observed bouton growth during LTP, the model predicted more growth on average than was found experimentally. This discrepancy could be explained by either incomplete incorporation of lost vesicles into the growing boutons or the possibility that some boutons within the LTP

←

vesicle numbers and bouton surface areas for control (***i***) and TBS (***j***) in the presence of 50 µM APV. ***k–l***, When treated with APV, neither vesicle numbers ($p = 0.67$; ***k***) nor bouton surface areas ($p = 0.12$; ***l***) were significantly altered with TBS. ***m***, Presynaptic vesicle numbers are positively correlated with bouton surface area in both control and TBS conditions in the presence of APV (Pearson's R, $p < 0.0001$). However, there was no difference in presynaptic vesicles across bouton sizes between conditions (ANCOVA: $F_{\mathrm{condition}} = 0.012$; df = 1; $p = 0.91$). For ***k–m***, n(Con + APV) = 66 and n(TBS + APV) = 67.

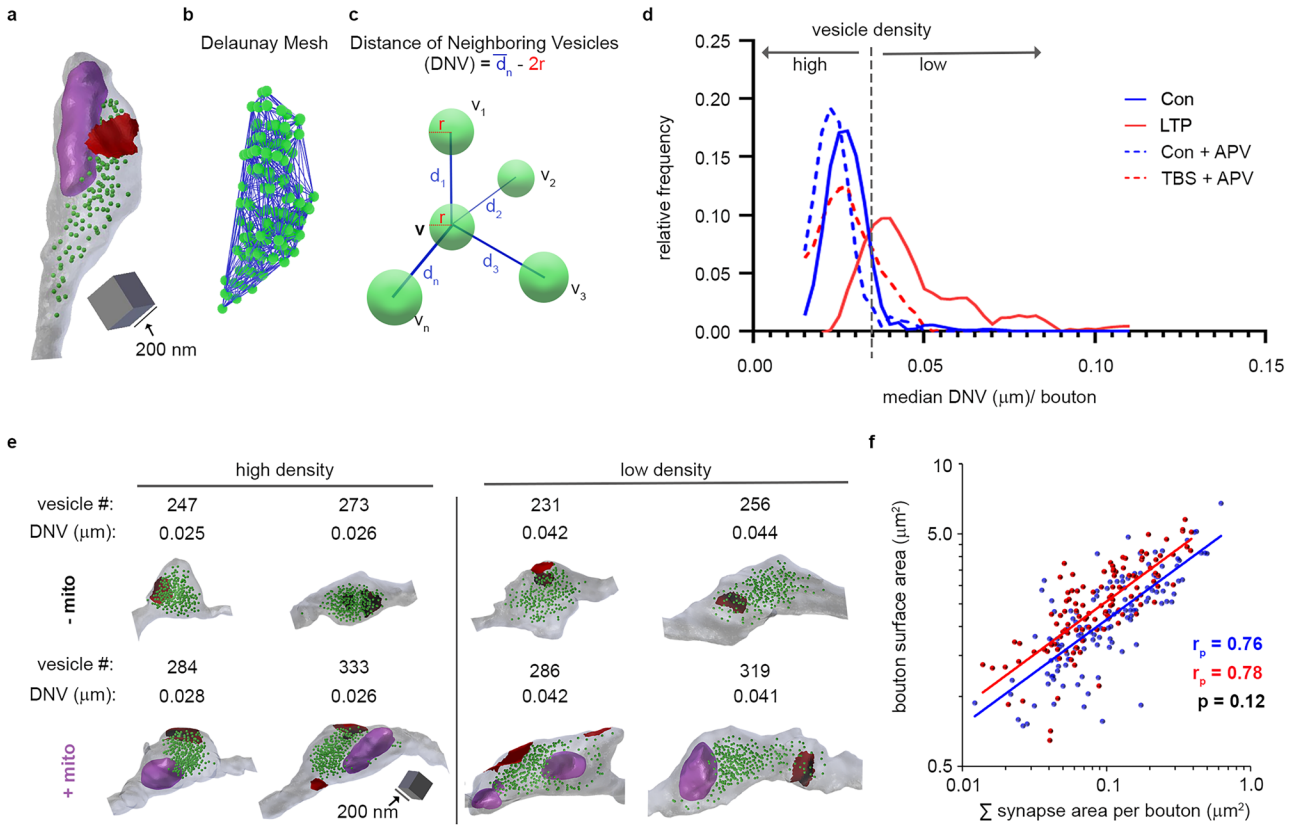

Figure 3. Decreased vesicle density is a feature of LTP. ***a***, Example 3D bouton with green vesicles, purple mitochondria, and red synapse. ***b***, Delaunay mesh connects the center points of vesicles in ***a*** to determine the distances of the neighboring vesicles. ***c***, Diagram showing how the average membrane to membrane distance to neighboring vesicles (DNV) was calculated for each vesicle. ***d***, The relative frequency of the median DNV per bouton is plotted for each condition. The dotted line at 0.035 µm indicates where the LTP and control lines intersect. Boutons with a median DNV $\geq$ 0.035 µm are classified as having a low vesicle density, and boutons with DNV < 0.035 µm have a high vesicle density. Most boutons in the LTP condition had low-density vesicles (77%), compared with the relatively few boutons in control, control-APV, and TBS-APV that had low-density vesicles (9, 6, 19%, respectively). ***e***, Example boutons with low and high vesicle densities that have similar vesicle numbers are shown, indicating that vesicle density is not merely a function of absolute vesicle number. Boutons can have high or low vesicle densities regardless of the presence of mitochondria. ***f***, Bouton surface areas are positively correlated with the total synapse area per bouton in both control high density boutons and LTP low vesicle density boutons (r_p = Pearson's R, $p < 0.0001$). However, there was no significant difference in bouton size across total synapse area between conditions ANCOVA: $F_{condition} = 2.38$; df = 1; $p = 0.12$; n(Control High Density) = 127 and n(LTP Low Density) = 118.

condition did not undergo vesicle loss and subsequent growth. To test the latter possibility, the data in our model were restricted to include only control boutons that had high-density vesicles (DNV < 0.035 µm) and LTP boutons that had low-density vesicles (DNV $\geq$ 0.035 µm) in accordance with the findings in Figure 3. These density-restricted bouton and summed vesicle surface areas were then plotted, and a new equation for lost vesicle surface area was derived from the regressions:

$$\text{Lost Vesicle SA } (\mu m^2) = y_{\text{Ctrl(high)}} - y_{\text{LTP(low)}},$$

where

$$y_{\text{Ctrl(high)}} = 2.24x - 2.27,$$

$$y_{\text{LTP(low)}} = 1.27x - 1.57,$$

$$\text{Lost Vesicle } SA \ (\mu m^2) = 0.963x - 0.703.$$

Adding the lost vesicle surface areas to the high-density control boutons resulted in a modeled growth regression that was statistically indistinguishable from the LTP low-density regression (Fig. 4*d*). Therefore, when vesicle density is used as an ultrastructural measure of potentiated boutons, our model supports the hypothesis that lost vesicles are building a bigger bouton during LTP. These novel findings suggest that decreased presynaptic vesicle density is a new structural identifier of potentiated boutons and supports a local mechanism for bouton enlargement.

Discussion

3DEM shows that presynaptic boutons enlarge as vesicle number decreases by 2 h following theta-burst stimulation (Bourne et al., 2013; Smith et al., 2016). Similarly, superresolution light microscopy shows bouton enlargement 1 h after high frequency stimulation induced LTP (Chéreau et al., 2017). Thus, bouton enlargement is a robust form of structural plasticity across different induction protocols and imaging modalities. Here we establish that LTP results in a decreased vesicle density in a subset of boutons. We show that these LTP low-density boutons have an increase in surface area that is commensurate with the surface area of the lost synaptic vesicles. This novel finding suggests a coordinated structural and functional change.

Individual hippocampal mammalian synapses exhibit a wide variation in the number of small synaptic vesicles, with a significant surplus beyond what is immediately required for synaptic transmission (Harris and Sultan, 1995). Vesicles that participate

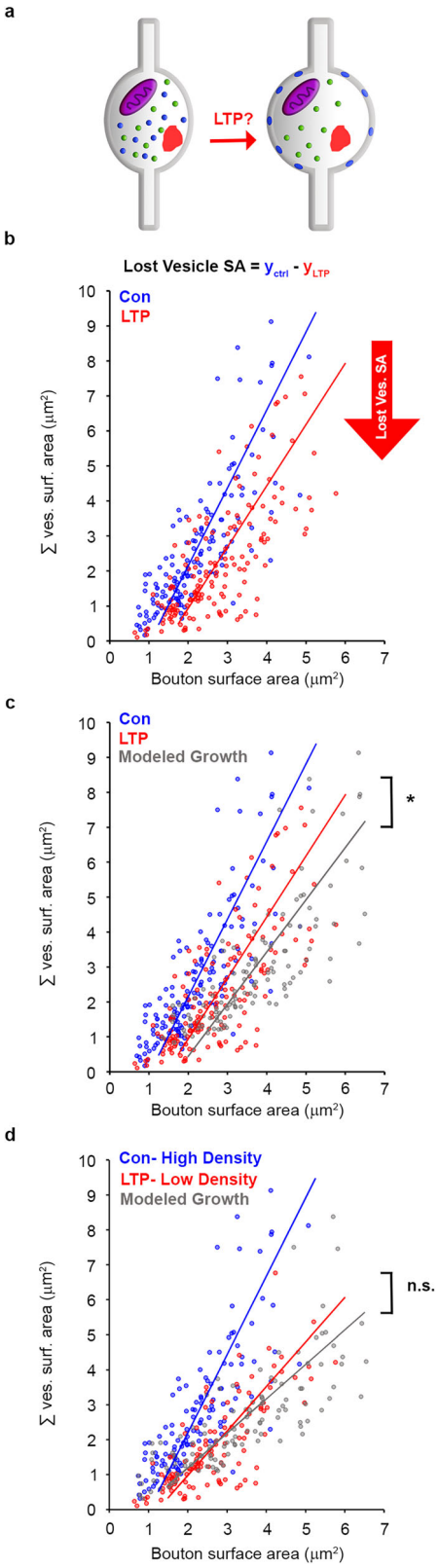

Figure 4. Modeling that includes vesicle density parameters accurately predicts bouton growth from the membrane of presynaptic vesicles lost during LTP. ***a***, Illustration demonstrating hypothesis that presynaptic vesicles lost during LTP (blue) provide the necessary membrane to grow presynaptic boutons (right). ***b***, Summed vesicle surface area plotted against bouton surface area with model II major axis linear regressions are shown for control and LTP. The equation for lost vesicle surface area with LTP was derived by subtracting the LTP regression from the control regression. ***c***, Modeled bouton growth during LTP was determined for each control bouton by using the equation derived in ***b*** to calculate the predicted summed vesicle surface area lost with LTP and adding it to the control bouton surface area. Modeled boutons and model II linear regression are shown in gray. Although the slopes for the modeled growth and LTP regressions do not differ ($p_{slope} = 0.69$), the intercepts are not equal ($p_{y\text{-intercept}} = 0.4$), indicating a poor model. ***d***, Control and LTP boutons were restricted to those that had high and low vesicle densities (respectively) as determined in Figure 3. When bouton growth was modeled as in ***b*** and ***c*** using only these restricted data, neither the regression slope nor the *y*-intercept of the modeled growth boutons differed from the LTP regression ($p_{slope} = 0.12$; $p_{y\text{-intercept}} = 0.20$).

in evoked release comprise the total recycling pool, which are functionally categorized into the readily releasable pool and the recycling pool (Alabi and Tsien, 2012; Chanaday et al., 2019). Synaptic vesicles that are resistant to release even during stimulation are referred to as the resting pool (Alabi and Tsien, 2012; Chanaday et al., 2019). Upon stimulation, vesicles in the readily releasable pool fuse with the plasma membrane, followed by the continued release of vesicles from the recycling pool after the readily releasable pool is depleted. Under baseline conditions, the resting pool does not participate in synaptic transmission. However, within 30 min of a potentiating stimuli, resting pool vesicles are recruited into the recycling pool (Ratnayaka et al., 2012; Rey et al., 2020). This recruitment process requires both NMDA receptor activation and nitric oxide signaling, indicating the necessity of postsynaptic activity and retrograde communication (Ratnayaka et al., 2012).

Within the resting pool, vesicles are interconnected by short filaments ~30 nm in length (Siksou et al., 2007; Cole et al., 2016). Synapsin I, a protein known to form similar 30 nm filaments, links synaptic vesicles to each other and to actin filaments (Hirokawa et al., 1989). In Synapsin null *Drosophila* larvae, 30% more vesicles become mobilized, indicating Synapsin as a potential marker for the resting pool of vesicles (Denker et al., 2011). Constitutive phosphorylation of Synapsin I by Cyclin-Dependent Kinase 5 (CDK5) enhances its binding to actin, effectively sequestering synaptic vesicles in the resting pool (Verstegen et al., 2014). Conversely, activity-dependent dephosphorylation of Synapsin I by Calcineurin and the subsequent release from actin filaments suggest a mechanism for mobilizing vesicles from the resting pool to the recycling pool upon neural activity (Ratnayaka et al., 2012; Verstegen et al., 2014). In this study, we identified vesicle density as a novel presynaptic structural marker of potentiation. Interestingly, the threshold used to categorize boutons as having high or low vesicle density was based on a distance to neighboring vesicles (DNV) of 35 nm, a value notably comparable to the length of Synapsin filaments. It is tempting to speculate that vesicles in the low-density boutons were mobilized by the activity-dependent dephosphorylation of Synapsin 1, recruiting vesicles from the resting pool to grow the bouton. While previous studies focused on recruitment of vesicles at earlier timepoints with LTP (≤30 min), this is the first evidence that similar dynamics may be at play during late-phase LTP (2 h).

To prevent the depletion of the vesicle pool, which would halt neurotransmission, exocytosis is tightly coupled with endocytosis. Following vesicle release at mammalian synapses, membrane is rapidly retrieved to maintain the vesicle pool through two main mechanisms (Chanaday et al., 2019). The first mechanism, ultrafast endocytosis, is a quick, localized process occurring on the millisecond timescale (Watanabe et al., 2013). The second mechanism, activity-dependent bulk endocytosis (ADBE), retrieves larger amounts of membrane over a few seconds (Clayton et

al., 2008). Interestingly, ADBE requires activity-dependent dephosphorylation of Dynamin I by Calcineurin (Xue et al., 2011), suggesting a shared mechanism with the previously described role of Calcineurin in mobilizing resting pool vesicles through Synapsin I dephosphorylation. If vesicle membrane is immediately retrieved after intense stimulation, then how does vesicle membrane remain within the plasma membrane to enlarge boutons with LTP? These results initially seem contradictory with the findings presented here. However, there are some key distinctions that could explain these phenomena. First, ADBE operates on a completely different timescale than late-phase LTP (seconds vs hours). This significant temporal difference suggests that ADBE, operating in the immediate aftermath of intense stimulation, likely serves a different homeostatic role than the longer-lasting structural changes observed during late-phase LTP. Second, the TBS protocol used to induce LTP in this study may engage different signaling pathways than the prolonged bursts of stimulation used to elicit ADBE (Clayton et al., 2008). Brain-derived neurotrophic factor (BDNF) is a well-known player in late-phase LTP, and its secretion is sensitive to alterations in stimulation paradigms, with LTP-producing stimuli eliciting increased BDNF release (Balkowiec and Katz, 2002; Aicardi et al., 2004). Interestingly, BDNF has been shown to prevent the rephosphorylation of Dynamin I, thereby inhibiting the rapid membrane retrieval mechanisms of ADBE (Smillie et al., 2013). This BDNF-mediated inhibition of ADBE represents one potential mechanism by which membrane retrieval might be modulated during longer-lasting plasticity, allowing for the incorporation of membrane necessary for the observed bouton enlargement. To our knowledge, there have not been any studies directly examining the mechanisms of endocytosis during LTP-inducing stimuli, whether it be TBS or HFS, leaving this an open area for future investigation.

Given the observed sustained bouton enlargement following LTP induction, it is important to understand its functional implications. Early modeling work suggested that alterations in axon geometries can influence action potential propagation by affecting its amplitude and width (Goldstein and Rall, 1974). More recently, modeling has demonstrated that increased axon diameter accelerates action potential conduction velocity between synaptic boutons; conversely, larger synaptic bouton or nonsynaptic varicosity sizes decelerate it (Chéreau et al., 2017; Griswold et al., 2025). Furthermore, activity-dependent plasticity has been shown to modulate action potential latency and amplitude hours after induction (Bakkum et al., 2008). Considering the importance of precise action potential timing for spike-timing dependent plasticity, changes in bouton size could represent a key mechanism for fine-tuning the arrival of these signals at postsynaptic sites. Beyond conduction velocity, bouton morphology also influences local calcium dynamics within the bouton and adjacent interbouton regions (Tran and Stricker, 2018), thereby having an impact on vesicle fusion and local signaling cascades that occur during plasticity. Thus, the LTP-induced bouton enlargement we observed likely contributes to both the temporal and biochemical modulation of synaptic transmission.

Our findings show no significant differences in the average cross-sectional area of the interbouton axonal shafts (based on total volume divided by length), suggesting the vesicle pool membrane is restricted to enlarging the synaptic boutons. This finding contrasts with Chéreau et al. (2017) who utilized live-cell STED imaging and found enlargement of the interbouton regions following LTP. This discrepancy might reflect differences in age, species, and tissue preparation (acute hippocampal slices from adult rats vs organotypic slices from young mice) and imaging resolution (EM vs STED). Recent work in hippocampal axons from young mice suggests that chemical fixation, compared with high-pressure freezing, diminishes nonsynaptic varicosities between boutons (Griswold et al., 2025). However, nonsynaptic varicosities that contain transport packets (i.e., <10 vesicles) are detected in our control aldehyde fixed tissue (Darcy et al., 2006; Bourne et al., 2013). Thus, multiple factors might contribute to the variability among studies regarding the interbouton morphology following LTP.

The proportional relationship between the presynaptic bouton and the area of the postsynaptic density was preserved across control and LTP conditions, even as boutons enlarged and vesicle counts and densities decreased. Prior work shows that smaller synapses have smaller vesicle pools with greater mobilization of vesicles from the resting pool to the recycling pool compared with boutons with larger synapses and vesicle pools (Ratnayaka et al., 2012; Rey et al., 2020). Thus, the smaller synapses on the low-density boutons likely correspond to boutons with higher vesicle mobilization. However, this mobilization occurs in a dynamic and coordinated manner that maintains scaling of bouton size across synapses of all sizes during LTP.

Whether enlarged boutons contribute to the remodeling of synaptic clusters near larger spines that have reached the final capacity for growth remains an open and compelling area for future investigation (Chirillo et al., 2019). Manual segmentation of vesicles in large-scale 3DEM datasets is tedious and provides a substantial hurdle to a more comprehensive circuit-level analyses needed to address these questions more generally. Although the incorporation of machine learning into 3DEM automatic segmentation pipelines has made many recent advances (Heinrich et al., 2021; Gallusser et al., 2022), accurate segmentation of synaptic vesicles remains challenging. Dysregulation of long-term presynaptic plasticity is emerging as an important player in several neuropsychiatric and neurodegenerative diseases (Monday and Castillo, 2017; Monday et al., 2018). This study reveals new evidence demonstrating the dynamic structural plasticity of presynaptic boutons, with significant implications for both normal brain function and neurological disorders.

Data Availability

All original datasets, analyses, metadata, and custom code along with instructions on how to view and access the data can be found at https://doi.org/10.18738/T8/UN9GUL.

References

Aicardi G, Argilli E, Cappello S, Santi S, Riccio M, Thoenen H, Canossa M (2004) Induction of long-term potentiation and depression is reflected by corresponding changes in secretion of endogenous brain-derived neurotrophic factor. Proc Natl Acad Sci U S A 101:15788–15792.

Alabi ARA, Tsien RW (2012) Synaptic vesicle pools and dynamics. Cold Spring Harb Perspect Biol 4:1–18.

Bakkum DJ, Chao ZC, Potter SM (2008) Long-term activity-dependent plasticity of action potential propagation delay and amplitude in cortical networks. PLoS One 3:e2088.

Balkowiec A, Katz DM (2002) Cellular mechanisms regulating activity-dependent release of native brain-derived neurotrophic factor from hippocampal neurons. J Neurosci 22:10399–10407.

Bartol TM, Keller DX, Kinney JP, Bajaj CL, Harris KM, Sejnowski TJ, Kennedy MB (2015) Computational reconstitution of spine calcium transients from individual proteins. Front Synaptic Neurosci 7:17.

Bliss T, Gardner-Medwin A (1973) Long-lasting potentiation of synaptic transmission in the dentate area of the unanaesthetized rabbit following stimulation of the perforant path. J Physiol 232:357–374.

Bourne JN, Harris KM (2011) Coordination of size and number of excitatory and inhibitory synapses results in a balanced structural plasticity along mature hippocampal CA1 dendrites during LTP. Hippocampus 21:354–373.

Bourne JN, Chirillo MA, Harris KM (2013) Presynaptic ultrastructural plasticity along CA3→CA1 axons during long-term potentiation in mature hippocampus. J Comp Neurol 521:3898–3912.

Buonarati OR, Hammes EA, Watson JF, Greger IH, Hell JW (2019) Mechanisms of postsynaptic localization of AMPA-type glutamate receptors and their regulation during long-term potentiation. Sci Signal 12: eaar6889.

Chanaday NL, Cousin MA, Milosevic I, Watanabe S, Morgan JR (2019) The synaptic vesicle cycle revisited: new insights into the modes and mechanisms' symposium and mini-symposium. J Neurosci 39:8209–8216.

Chéreau R, Ezequiel Saraceno G, Angibaud J, Cattaert D, Valentin Nägerl U (2017) Superresolution imaging reveals activity-dependent plasticity of axon morphology linked to changes in action potential conduction velocity. Proc Natl Acad Sci U S A 114:1401–1406.

Chirillo MA, Waters MS, Lindsey LF, Bourne JN, Harris KM (2019) Local resources of polyribosomes and SER promote synapse enlargement and spine clustering after long-term potentiation in adult rat hippocampus. Sci Rep 9:1–14.

Chirillo MA, Falco JN, Musslewhite MD, Lindsey LF, Harris KM (2025) "PyReconstruct: A Fully Opensource, Collaborative Successor to Reconstruct." Preprint, bioRxiv, April 22.

Choquet D (2018) Linking nanoscale dynamics of AMPA receptor organization to plasticity of excitatory synapses and learning' viewpoints. J Neurosci 38:9318–9329.

Clayton EL, Evans GJO, Cousin MA (2008) Bulk synaptic vesicle endocytosis is rapidly triggered during strong stimulation' brief communications. J Neurosci 28:6627–6632.

Cole AA, Chen X, Reese TS (2016) A network of three types of filaments organizes synaptic vesicles for storage, mobilization, and docking. J Neurosci 36:3222–3230.

Darcy KJ, Staras K, Collinson LM, Goda Y (2006) Constitutive sharing of recycling synaptic vesicles between presynaptic boutons. Nat Neurosci 9:315–321.

Denker A, Bethani I, Kröhnert K, Körber C, Horstmann H, Wilhelm B, Barysch S, Kuner T, Neher E, Rizzoli S (2011) A small pool of vesicles maintains synaptic activity in vivo. Proc Natl Acad Sci U S A 108: 17177–17182.

Fernandez-Alfonso T, Ryan TA (2008) A heterogeneous 'resting' pool of synaptic vesicles that is dynamically interchanged across boutons in mammalian CNS synapses. Brain Cell Biol 36:87–100.

Fiala JC (2005) *Reconstruct*: a free editor for serial section microscopy. J Microsc 218:52–61.

Fiala JC, Harris KM (2001) Extending unbiased stereology of brain ultrastructure to three-dimensional volumes. J Am Med Inform Assoc 8:1–16.

Fiala JC, Kirov SA, Feinberg MD, Petrak LJ, George P, Goddard CA, Harris KM (2003) Timing of neuronal and glial ultrastructure disruption during brain slice preparation and recovery in vitro. J Comp Neurol 465:90–103.

Gallusser B, Maltese G, Di Caprio G, Vadakkan TJ, Sanyal A, Somerville E, Sahasrabudhe M, O'Connor J, Wigert M, Kirchhausen T (2022) Deep neural network automated segmentation of cellular structures in volume electron microscopy. J Cell Biol 222:e202208005.

Goldstein SS, Rall W (1974) Changes of action potential shape and velocity for changing core conductor geometry. Biophys J 14:731–757.

Griswold JM, et al. (2025) Membrane mechanics dictate axonal pearls-on-a-string morphology and function. Nat Neurosci 28:49–61.

Harris KM (2025) Enhanced cycling of presynaptic vesicles during long-term potentiation in rat hippocampus. J Physiol 603:6001–6013.

Harris KM, Sultan P (1995) Variation in the number, location and size of synaptic vesicles provides an anatomical basis for the nonuniform probability of release at hippocampal CA1 synapses. Neuropharmacology 34: 1387–1395.

Harris KM, Spacek J, Bell ME, Parker PH, Lindsey LF, Baden AD, Vogelstein JT, Burns R (2015) A resource from 3D electron microscopy of hippocampal neuropil for user training and tool development. Sci Data 2:150046.

Heinrich L, et al. (2021) Whole-cell organelle segmentation in volume electron microscopy. Nature 599:141–146.

Hirokawa N, Sobue K, Kanda K, Harada A, Yorifuji H (1989) The cytoskeletal architecture of the presynaptic terminal and molecular structure of synapsin 1. J Cell Biol 108:111–126.

Jung JH, Kirk LM, Bourne JN, Harris KM (2021) Shortened tethering filaments stabilize presynaptic vesicles in support of elevated release probability during LTP in rat hippocampus. Proc Natl Acad Sci U S A 118:1–8.

Meyer D, Bonhoeffer T, Scheuss V (2014) Balance and stability of synaptic structures during synaptic plasticity. Neuron 82:430–443.

Monday HR, Castillo PE (2017) Closing the gap: long-term presynaptic plasticity in brain function and disease. Curr Opin Neurobiol 45:106–112.

Monday HR, Younts TJ, Castillo PE (2018) Long-term plasticity of neurotransmitter release: emerging mechanisms and contributions to brain function and disease. Annu Rev Neurosci 41:299–322.

Neher E, Brose N (2018) Dynamically primed synaptic vesicle states: key to understand synaptic short-term plasticity. Neuron 100:1283–1291.

Ratnayaka A, Marra V, Bush D, Burden JJ, Branco T, Staras K (2012) Recruitment of resting vesicles into recycling pools supports NMDA receptor-dependent synaptic potentiation in cultured hippocampal neurons. J Physiol 590:1585–1597.

Rey S, Marra V, Smith C, Staras K (2020) Nanoscale remodeling of functional synaptic vesicle pools in Hebbian plasticity. Cell Rep 30: 2006–2017.e3.

Siksou L, et al. (2007) Three-dimensional architecture of presynaptic terminal cytomatrix. J Neurosci 27:6868–6877.

Smillie KJ, Pawson J, Perkins EM, Jackson M, Cousin MA (2013) Control of synaptic vesicle endocytosis by an extracellular signalling molecule. Nat Commun 4:2394.

Smith HL, Bourne JN, Cao G, Chirillo MA, Ostroff LE, Watson DJ, Harris KM (2016) Mitochondrial support of persistent presynaptic vesicle mobilization with age-dependent synaptic growth after LTP. Elife 5:1–30.

Sokolov MV, Rossokhin AV, Astrelin AV, Frey JU, Voronin LL (2002) Quantal analysis suggests strong involvement of presynaptic mechanisms during the initial 3 h maintenance of long-term potentiation in rat hippocampal CA1 area in vitro. Brain Res 957:61–75.

Tran V, Stricker C (2018) Diffusion of Ca^{2+} from small boutons en passant into the axon shapes AP-evoked Ca^{2+} transients. Biophys J 115:1344–1356.

Verstegen AMJ, et al. (2014) Phosphorylation of synapsin I by cyclin-dependent kinase-5 sets the ratio between the resting and recycling pools of synaptic vesicles at hippocampal synapses. J Neurosci 34:7266–7280.

Watanabe S, Rost BR, Camacho-Pérez M, Davis MW, Söhl-Kielczynski B, Rosenmund C, Jorgensen EM (2013) Ultrafast endocytosis at mouse hippocampal synapses. Nature 504:242–247.

Xue J, Graham ME, Novelle AE, Sue N, Gray N, McNiven MA, Smillie KJ, Cousin MA, Robinson PJ (2011) Calcineurin selectively docks with the dynamin Ixb splice variant to regulate activity-dependent bulk endocytosis. J Biol Chem 286:30295–30303.